Haibo Li
State Key Laboratory of Ocean Engineering,
School of Naval Architecture, Ocean and Civil Engineering,
Shanghai Jiao Tong University,
Shanghai 200240, China;
Department of Civil and Environmental Engineering;
Department of Mechanical Engineering;
Department of Materials Science and Engineering,
Northwestern University,
Evanston, IL 60208

Xi Wang
State Key Laboratory of Ocean Engineering,
School of Naval Architecture, Ocean and Civil Engineering,
Shanghai Jiao Tong University,
Shanghai 200240, China

Feng Zhu
Department of Civil and Environmental Engineering;
Department of Mechanical Engineering;
Department of Materials Science and Engineering,
Northwestern University,
Evanston, IL 60208;
School of Logistics Engineering,
Wuhan University of Technology,
Wuhan 430063, China

Xin Ning[1]
Department of Materials Science and Engineering,
Frederick Seitz Materials Research Laboratory,
University of Illinois at Urbana-Champaign,
Urbana, IL 61801

Heling Wang[2]
Department of Civil and Environmental Engineering;
Department of Mechanical Engineering;
Department of Materials Science and Engineering,
Northwestern University,
Evanston, IL 60208
e-mail: heling.wang@northwestern.edu

John A. Rogers
Department of Materials Science and Engineering;
Department of Biomedical Engineering;
Department of Chemistry;
Department of Mechanical Engineering;
Department of Electrical Engineering and Computer Science;
Department of Neurological Surgery,
Center for Bio-Integrated Electronics,
Simpson Querrey Institute for BioNanotechnology,
McCormick School of Engineering and
Feinberg School of Medicine,
Northwestern University,
Evanston, IL 60208

Yihui Zhang
Center for Flexible Electronics Technology and
Center for Mechanics and Materials,
Beijing 100084, China;
AML, Department of Engineering Mechanics,
Tsinghua University,
Beijing 100084, China

Yonggang Huang
Department of Civil and Environmental Engineering;
Department of Mechanical Engineering;
Department of Materials Science and Engineering;
Center for Bio-Integrated Electronics,
Northwestern University,
Evanston, IL 60208

Viscoelastic Characteristics of Mechanically Assembled Three-Dimensional Structures Formed by Compressive Buckling

Vibrational microplatforms that exploit complex three-dimensional (3D) architectures assembled via the controlled compressive buckling technique represent promising candidates in 3D micro-electromechanical systems (MEMS), with a wide range of applications such as oscillators, actuators, energy harvesters, etc. However, the accuracy and efficiency of such 3D MEMS might be significantly reduced by the viscoelastic damping effect that arises from material viscosity. Therefore, a clear understanding and characterization of such effects are essential to progress in this area. Here, we present a study on the viscoelastic damping effect in complex 3D structures via an analytical model and finite element analysis (FEA). By adopting the Kelvin–Voigt model to characterize the material viscoelasticity, an analytical solution is derived for the vibration of a buckled ribbon. This solution then yields a scaling law for the half-band width or the quality factor of vibration that can be extended to other classes of complex 3D structures, as validated by FEA. The scaling law reveals the dependence of the half-band width on the geometries of 3D structures and the compressive strain. The results could serve as guidelines to design novel 3D vibrational microplatforms for applications in MEMS and other areas of technology. [DOI: 10.1115/1.4041163]

Keywords: viscoelasticity, half-band width, controlled compressive buckling, complex three-dimensional structure

[1]Present address: Department of Aerospace Engineering, The Pennsylvania State University, University Park, PA 16802
[2]Corresponding author.

Contributed by the Applied Mechanics Division of ASME for publication in the Journal of Applied Mechanics. Manuscript received July 9, 2018; final manuscript received August 5, 2018; published online August 31, 2018. Assoc. Editor: Pradeep Sharma.

1 Introduction

Micro- and nanostructures in micro-electromechanical systems (MEMS) are of significant current research interest, due partly to their relevance to wide ranging classes of applications in biomedicine [1–3], sensors [4–6], electronics and optoelectronics [7–9], batteries and supercapacitors [10–12], robotics [13–15], and others [16,17]. In MEMS, structural vibration plays a key role in the transformation from mechanical signals to electrical signals [18,19]. The utilization of three-dimensional (3D) micro- and nanostructures provide significant advantages and design flexibility compared to those based on two-dimensional (2D) structures [20–23], especially in areas of energy harvesting, sensing of anisotropic mechanical properties, and simultaneous evaluation of multiple mechanical properties (density, modulus, etc.), due to their ability to support multidirectional vibrations and controlled vibration modes [24].

Diverse manufacturing techniques based on phenomena such as mechanical buckling [25–28], self-folding induced by residual stress [29–32], surface instabilities [33–35], capillary forces [36–38], and temperature changes [39,40] can provide access to 3D micro- and nanostructures. Among these methods, the compressive buckling approach is notable for its ability to construct complex 3D structures with vibration behaviors (e.g., natural frequency) that can be tuned by applying tensile strain to the soft, elastomeric assembly platform. In addition, this technique is compatible with a variety of active materials, such as poly (vinylidene fluoride), $Pb(Zr,Ti)O_3$ (PZT), and conductive metals, allowing actuation by external stimuli based on electric and/or magnetic fields. Such options provide great potential in the applications of resonators, energy harvesters, and other systems based on continuous adaption of the resonant frequency or vibration modes [24].

One major challenge in the design of 3D MEMS arises from the effects of viscoelasticity in the constituent materials. Such effects lead to dissipation of energy, changes in stress distributions, displacements, and frequencies during vibration [41–45]. For example, increases in the ambient temperature and/or humidity can increase the viscosity [46–48], which, in turn, can reduce the efficiency of 3D MEMS devices. The viscoelastic properties can be characterized by dynamic mechanical analysis [49] and creep and stress relaxation methods [50] for a wide range of materials, such as poly(methyl methacrylate), SU8 epoxy resin, polypropylene, polydimethylsiloxane, etc. [51–55]. The viscoelastic damping effect due to viscosity of materials in a vibration system can be characterized by the half bandwidth ξ or the quality factor Q ($Q = 1/(2\xi)$) [56–58].

Several viscoelastic models have been proposed to characterize the viscoelastic material properties including Maxwell model, Kelvin–Voigt model, and standard linear solid model [59–61]. Among them, the Kelvin–Voigt model is a classical and widely used viscoelastic model. For example, Ghayesh [62] investigated the nonlinear dynamic response of a simply supported beam supported by a nonlinear spring. Mahmoodi et al. [63] reported the experimental study of nonlinear vibration and frequency responses of viscoelastic beams, with good agreement between experimental results and numerical simulations. Kolahchi [64] studied the nonlinear vibrations of viscoelastic rectangular plates. These investigations focus on the viscoelastic damping effect of 2D plates or beams. Though Tseng and Dugundji [65] investigated the vibration of a buckled beam, they only provided an exact solution for the case without viscoelastic damping. Similarly, Cottone et al. [66] studied piezoelectric buckled beams as a vibration energy harvester. The aforementioned theoretical models are restricted to a few simple geometries and cannot be directly extended to complex 3D structures. Therefore, it is important to develop a theoretical model to predict the viscoelastic damping effect of vibrations in complex 3D structures.

This paper presents a study on the viscoelastic characteristics of 3D mechanically assembled structures formed by compressive buckling techniques via an analytical model and finite element analysis (FEA). The Kelvin–Voigt model is used to capture the viscoelastic effects of conventional materials (SU8, PVDF, etc.) in these structures. An analytical model explicitly relates the half-band width of a buckled ribbon to the geometry/material parameters and the compressive strain. Then, a more general model describes the half-band width of complex structures, with two fitting parameters to account for the complexity of the vibration mode and structure. The models are validated by FEA with good agreement. They provide insights into the effect of design parameters (material, compressive strain, structure shape, etc.) on the vibration behavior and may serve as useful references in the design of 3D vibrational platforms and the potential applications of 3D MEMS.

2 The Viscoelastic Characteristics of Three-Dimensional Buckled Ribbon and Three-Dimensional Structures

A schematic illustration of a buckled ribbon excited by an external harmonic load is shown in Fig. 1. A straight 2D slender ribbon (length L, width b, and thickness h) is selectively bonded to a highly prestrained elastomer at two ends as shown in Fig. 1(*a*). Release of the prestrain induces compression and triggers buckling of the ribbon into the arch shape, as shown in Fig. 1(*b*), where l represents the distance between two bonding sites after compression. Considering that the viscosity of the soft elastomer may increase the half-band width of vibration, the buckled ribbon is transferred on to a rigid base using the technique reported by Yan et al. [67]. An external harmonic load (see Fig. 1(*c*)) then actuates the first-order vibration mode shown in Fig. 1(*d*). Because of the base has larger modulus than the buckled ribbon, its deformation can be neglected during the vibration analysis. Due to the ribbon thickness (h) is much smaller than its width (b) and length (L), finite-deformation beam theory with no shear deformation [68–70] is adopted to establish an analytical model. In general, the deformations of a planar ribbon can be described by the displacement of the central axis $\boldsymbol{u} = u_i\boldsymbol{E_i}$ [71] and the twist angle ψ [68], where $\boldsymbol{E_i}$ is the unit vector before deformation in the Cartesian coordinates (X, Y, Z), which all calculations are based on. For the post-buckling and vibration shown in Fig. 1, only the displacement components in the X–Z plane are involved.

2.1 The Construction of Governing Equations. For a moderate level of compressive strain (e.g., $<30\%$), the displacements of the ribbon after the post-buckling could be expressed as [24,72,73]

$$u_{1(0)} = A_{(0)}\left[\cos\left(\frac{2\pi}{L}Z\right)+1\right],\ u_{3(0)} = \frac{\pi A_{(0)}^2}{4L}\sin\left(\frac{4\pi}{L}Z\right) - \varepsilon_{\text{compre}}Z \tag{1}$$

where $\varepsilon_{\text{compre}} = L - l/L$ is the relative dimensional change between the two bonding sites, or called the compressive strain; $\varepsilon_{\text{compre}}$ is related to the elastomer prestrain $\varepsilon_{\text{prestrain}}$ via $\varepsilon_{compre} = \varepsilon_{\text{prestrain}}/(1+\varepsilon_{\text{prestrain}})$; $\varepsilon_{\text{c}} = \pi^2h^2/(3L^2)$ is the critical strain; and $A_{(0)} = \sqrt{(3L^2\varepsilon_{\text{compre}} - \pi^2h^2)/3\pi^2} = L/\pi\sqrt{\varepsilon_{\text{compre}} - \varepsilon_{\text{c}}}$ is the static deflection amplitude of the buckled ribbon. Due to the rigidity of the fix stage, the boundary conditions are

$$u_1(\pm L/2) = 0,\ u_3(\pm L/2) = 0,\ \frac{\mathrm{d}u_1}{\mathrm{d}Z}(\pm L/2) = 0 \tag{2}$$

Then a vibration displacement function $\Delta u_i(Z,t)$ is superimposed on $u_{i(0)}(Z)$ to give the total displacement of the buckled ribbon as

$$u_1(Z,t) = u_{1(0)} + \Delta u_1(Z,t),\quad u_3(Z,t) = u_{3(0)} + \Delta u_3(Z,t) \tag{3}$$

By introducing a set of series $\varphi_{(k)}(Z)$ and $\phi_{(k)}(Z)$ into the vibration displacements, the total displacements of the buckled ribbon can be further written as

$$u_1(Z,t) = u_{1(0)} + \Delta u_1(Z,t) = u_{1(0)} + \sum_{k=1}^{n} \Delta a_{(k)}(t)\varphi_{(k)}(Z) \quad (4)$$

$$u_3(Z,t) = u_{3(0)} + \Delta u_3(Z,t) = u_{3(0)} + \sum_{k=1}^{n} \Delta a_{(k)}(t)\phi_{(k)}(Z) \quad (5)$$

The total displacements should satisfy the boundary conditions in Eq. (2), leading to

$$\varphi_{(k)}(\pm L/2) = 0,\ \phi_{(k)}(\pm L/2) = 0 \ \text{and} \ \frac{d\varphi_k}{dZ}(\pm L/2) = 0 \quad (6)$$

To describe the viscoelastic characteristics of the buckled ribbon, the physical relationship for Kelvin–Voigt model is introduced as

$$\sigma = \sigma^e + \sigma^d = E\varepsilon(X,Z,t) + \eta E \frac{\partial \varepsilon(X,Z,t)}{\partial t} \quad (7)$$

where σ is the stress, ε is the strain, and E and η are the elastic modulus and viscoelastic damping coefficient of the ribbon material, respectively. According to the beam theory

$$\varepsilon = (\lambda - 1) - X\kappa \quad (8)$$

where λ is the stretch ratio and κ is the curvature. Noe that X represents the distance from a point on the cross section to the central axis of the ribbon, where the origin of the coordinate system locates at.

To solve $\Delta a_{(k)}(t)$ in Eqs. (4) and (5), the Lagrange's equation of motion is introduced. Specifically, the strain energy W_s of the buckled ribbon is given by [74]

$$W_s = \frac{1}{2}\int_{-L/2}^{L/2} Ebh(\lambda - 1)^2 dZ + \frac{1}{24}\int_{-L/2}^{L/2} Ebh^3\kappa^2 dZ \quad (9)$$

By neglecting the terms of the third and higher order power of $\Delta \boldsymbol{a}$ in Eq. (9), the potential energy can be also written as $W_s = 1/2\Delta\boldsymbol{a}^T\boldsymbol{K}\Delta\boldsymbol{a}$, in which $\Delta\boldsymbol{a}$ is a $n\times 1$ vector $\{\Delta a_{(1)}, \Delta a_{(2)}, \ldots, \Delta a_{(n)}\}^T$, and $\boldsymbol{K}$ is an $n \times n$ stiffness matrix. Similarly, the kinetic energy can be given as

$$T(\Delta\dot{\boldsymbol{a}}) = \frac{1}{2}\int_{-L/2}^{L/2} \rho bh\left[\left(\frac{\partial u_{1(v)}}{\partial t}\right)^2 + \left(\frac{\partial u_{3(v)}}{\partial t}\right)^2\right] dZ = \frac{1}{2}\Delta\dot{\boldsymbol{a}}^T\boldsymbol{M}\Delta\dot{\boldsymbol{a}} \quad (10)$$

where $\Delta\dot{\boldsymbol{a}} = \{\Delta\dot{a}_{(1)}, \Delta\dot{a}_{(2)}, \ldots, \Delta\dot{a}_{(n)}\}^T$ is the time derivative of $\Delta\boldsymbol{a}$, i.e., $\Delta\dot{\boldsymbol{a}} = d(\Delta\boldsymbol{a})/dt$, ρ is the density of the ribbon material, and $\boldsymbol{M}$ is an $n \times n$ mass matrix.

Based on Eq. (7), the dissipation function of the buckled ribbon can be obtained as follows:

$$D = \frac{1}{2}\int_{-L/2}^{L/2} \eta Ebh\left(\frac{\partial\lambda}{\partial t}\right)^2 dZ + \frac{1}{24}\int_{-L/2}^{L/2} \eta Ebh^3\left(\frac{\partial\kappa}{\partial t}\right)^2 dZ \quad (11)$$

The potential energy of the external harmonic load can be written as

$$W_{ext} = -\int_{-L/2}^{L/2} P(t)\Delta u_1(Z,t)dZ \quad (12)$$

where $P(t)$ is the external force exerted on per unit length of bucked ribbon and ω is the frequency of the external harmonic load.

The Lagrange's equation of motion requires that

$$\frac{\partial(T - W_s)}{\partial\Delta\boldsymbol{a}} - \frac{d}{dt}\frac{\partial(T - W_s)}{\partial\Delta\dot{\boldsymbol{a}}} - \frac{\partial D}{\partial\Delta\dot{\boldsymbol{a}}} - \frac{\partial W_{ext}}{\partial\Delta\boldsymbol{a}} = 0 \quad (13)$$

By substituting Eqs. (7)–(12) into Eq. (13), the governing equation of the buckled ribbon under an external harmonic load is obtained as

$$\boldsymbol{M}\Delta\ddot{\boldsymbol{a}} + \boldsymbol{C}\Delta\dot{\boldsymbol{a}} + \boldsymbol{K}\Delta\boldsymbol{a} = \boldsymbol{F} \quad (14)$$

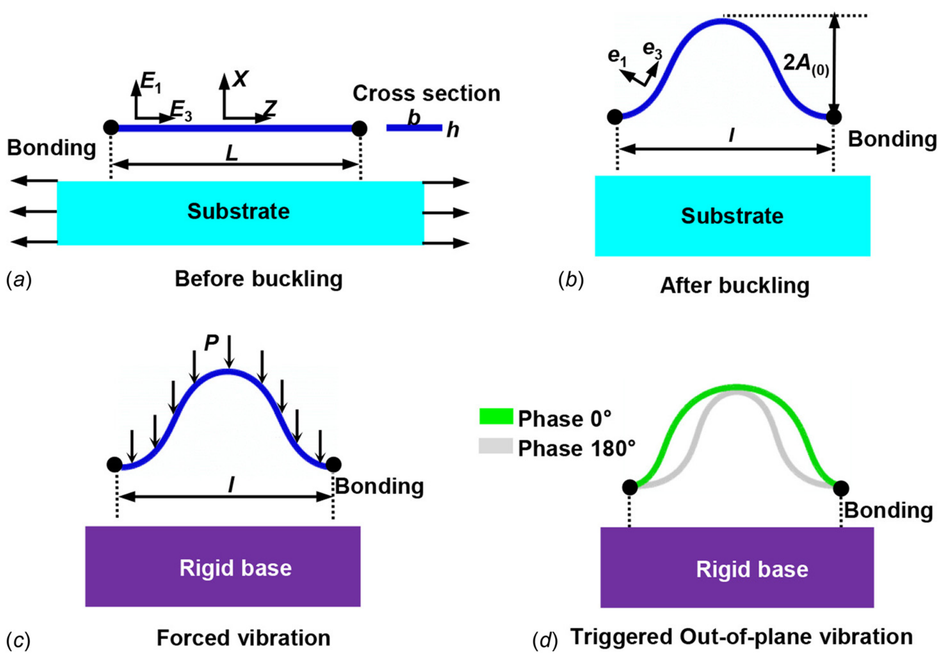

Fig. 1 Illustration of (*a*) a straight ribbon attached to a prestrained substrate at selected bonding sites, (*b*) the compressive post-buckling induced by the contraction of the elastomer, (*c*) the external load, and (*d*) the first-order vibration mode. Two phases corresponding to the largest vibration amplitudes are shown, i.e., up line: phase 0 deg, down line: phase 180 deg.

2.2 The Half-Band Width of the First-Order Vibration Mode. For the first-order vibration mode excited by the external harmonic load, FEA results show that the vibration displacement can be well characterized by superposition of the following base functions, with two terms (i.e., $n = 2$) in Eqs. (4) and (5), as [24]:

$$\varphi_{(1)}(Z) = 1 + \cos\left(\frac{2\pi Z}{L}\right), \quad \varphi_{(2)}(Z) = 1 - \cos\left(\frac{4\pi Z}{L}\right) \tag{15}$$

$$\phi_{(1)}(Z) = \frac{\pi A_{(0)}}{2L}\sin\left(\frac{4\pi Z}{L}\right),$$
$$\phi_{(2)}(Z) = \frac{\pi A_{(0)}}{3L}\left[6\sin\left(\frac{2\pi Z}{L}\right) - 2\sin\left(\frac{6\pi Z}{L}\right)\right] \tag{16}$$

The potential energy of the vibration is then derived as

$$W_s = \frac{Ebh^3}{L^3}\left(k_{11}\Delta a_{(1)}^2 + k_{22}\Delta a_{(2)}^2\right) \tag{17}$$

where

$$k_{11} = -\frac{5\pi^6 A_{(0)}^2}{3L^2} + \frac{2\pi^4 A_{(0)}^2}{h^2} \text{ and } k_{22} = \frac{28\pi^6 A_{(0)}^2}{3L^2} + 4\pi^4 \tag{18}$$

The kinetic energy is then written as

$$T = \rho bhL\left(m_{11}\Delta\dot{a}_{(1)}^2 + m_{22}\Delta\dot{a}_{(2)}^2 + m_{12}\Delta\dot{a}_{(1)}\Delta\dot{a}_{(2)}\right) \tag{19}$$

where

$$m_{11} = \frac{\pi^2 A_{(0)}^2}{16L^2} + \frac{3}{4}, m_{22} = \frac{10\pi^2 A_{(0)}^2}{9L^2} + \frac{3}{4}, m_{12} = 1 \tag{20}$$

The dissipation function is calculated as

$$D = \frac{\pi^4 \eta Ebh^3}{3L^3}\left(c_{11}\Delta\dot{a}_{(1)}^2 + c_{22}\Delta\dot{a}_{(2)}^2\right) \tag{21}$$

where

$$c_{11} = -\frac{\pi^2 A_{(0)}^2}{L^2} + \frac{6A_{(0)}^2}{h^2} + 1, \; c_{22} = \frac{32\pi^2 A_{(0)}^2}{L^2} + 16 \tag{22}$$

A harmonic load $P(t) = P_0\sin(\omega t)$ is exerted on the ribbon leading to the potential energy as

$$W_{\text{ext}} = -P_0 L\left(\Delta a_{(1)} + \Delta a_{(2)}\right)\sin(\omega t) \tag{23}$$

Substitution of Eqs. (17)–(23) into Eq. (13) gives the governing equations

$$\begin{bmatrix} M_{11} & M_{12} \\ M_{12} & M_{22} \end{bmatrix}\begin{bmatrix} \Delta\ddot{a}_{(1)} \\ \Delta\ddot{a}_{(2)} \end{bmatrix} + \begin{bmatrix} C_{11} & 0 \\ 0 & C_{22} \end{bmatrix}\begin{bmatrix} \Delta\dot{a}_{(1)} \\ \Delta\dot{a}_{(2)} \end{bmatrix} + \begin{bmatrix} K_{11} & 0 \\ 0 & K_{22} \end{bmatrix}\begin{bmatrix} \Delta a_{(1)} \\ \Delta a_{(2)} \end{bmatrix} = \begin{bmatrix} P_0 L\sin(\omega t) \\ P_0 L\sin(\omega t) \end{bmatrix} \tag{24}$$

where

$$M_{11} = 2\rho bhLm_{11},\; M_{22} = 2\rho bhLm_{22},\; M_{12} = \rho bhLm_{12}$$
$$C_{11} = \frac{2\pi^4\eta Ebh^3}{3L^3}c_{11},\; C_{22} = \frac{2\pi^4\eta Ebh^3}{3L^3}c_{22} \tag{25}$$
$$K_{11} = \frac{2Ebh^3}{L^3}k_{11},\; K_{22} = \frac{2Ebh^3}{L^3}k_{22}$$

The solutions to Eq. (24) are

$$\begin{bmatrix} \Delta a_{(1)} \\ \Delta a_{(2)} \end{bmatrix} = \begin{bmatrix} B_1\sin(\omega t + \theta_1) \\ B_2\sin(\omega t + \theta_2) \end{bmatrix} \tag{26}$$

with the specific deducing process and the expressions of B_1, B_2, θ_1, θ_2 presented in the Appendix.

Therefore, the transverse vibrational displacement and velocity of the buckled ribbon can be written as

$$\Delta u_1(Z,t) = \Delta a_{(1)}\varphi_{(1)}(Z) + \Delta a_{(2)}\varphi_{(2)}(Z) = B(Z,\omega)\sin(\omega t + \theta) \tag{27}$$

$$v_1(Z,t) = \omega B(Z,\omega)\cos(\omega t + \theta) \tag{28}$$

where

$$B = \sqrt{\left[B_{r1}(\omega)\varphi_{(1)}(Z) + B_{r2}(\omega)\varphi_{(2)}(Z)\right]^2 + \left[B_{i1}(\omega)\varphi_{(1)}(Z) + B_{i2}(\omega)\varphi_{(2)}(Z)\right]^2}$$
$$\tan\theta = \left[B_{i1}(\omega)\varphi_{(1)}(Z) + B_{i2}(\omega)\varphi_{(2)}(Z)\right]/\left[B_{r1}(\omega)\varphi_{(1)}(Z) + B_{r2}(\omega)\varphi_{(2)}(Z)\right] \tag{29}$$

with B_{r1}, B_{r2}, B_{i1}, and B_{i2} presented in the Appendix. In Eq. (27), $B(Z, \omega)$ is the spatial part of the transverse vibrational displacement and the vibration amplitude $A(\omega)$ is defined as the maximum of B with respective to the position Z. At a given position, the normalized vibrational velocity as a function of the frequency is

$$\mu(\omega) = \frac{2\omega BEbh^3}{P_0 L^4} \tag{30}$$

The half-band width of the buckled ribbon is

$$\xi = \frac{\omega_2 - \omega_1}{2\omega_0} \tag{31}$$

where ω_0 is the resonant frequency, i.e., the frequency at which $\mu(\omega)$ reaches its maximum $\mu_{\max}$; ω_1 and ω_2 are the two solutions to $\mu(\omega) = \mu_{\max}/\sqrt{2}$. We refer to Eq. (31) as the general form of the analytical model.

It is verified that $\varphi_{(1)}(Z)$ and $\phi_{(1)}(Z)$ in Eqs. (15) and (16) could dominate the vibration mode, when the static deflection amplitude of the buckled ribbon is much smaller than the ribbon thickness, i.e., $A_{(0)} \ll h$, while $\varphi_{(2)}(Z)$ and $\phi_{(2)}(Z)$ could dominate the vibration mode when $A_{(0)} \gg h$. Then, the vibration velocity in Eq. (30) could be degenerated to

$$\mu^* = \frac{\omega}{\sqrt{\left(-\omega^2\cdot M_{11} + K_{11}\right)^2 + \left(\omega\cdot C_{11}\right)^2}} \quad (A_{(0)} \ll h) \tag{32}$$

$$\mu^* = \frac{\omega}{\sqrt{(-\omega^2 \cdot M_{22} + K_{22})^2 + (\omega \cdot C_{22})^2}} \quad (A_{(0)} \gg h) \tag{33}$$

which lead to the half-band width

$$\xi^* = \frac{\omega_2 - \omega_1}{2\omega_0} = \frac{C_{11}}{2\sqrt{M_{11}K_{11}}} = \frac{\pi^4 \eta h}{6L^2}\sqrt{\frac{E}{\rho}}\frac{c_{11}}{\sqrt{m_{11}k_{11}}} = \frac{\pi^4 \eta \omega_0}{6}\frac{c_{11}}{k_{11}} \quad (A_{(0)} \ll h) \tag{34}$$

$$\xi^* = \frac{\omega_2 - \omega_1}{2\omega_0} = \frac{C_{22}}{2\sqrt{M_{22}K_{22}}} = \frac{\pi^4 \eta h}{6L^2}\sqrt{\frac{E}{\rho}}\frac{c_{22}}{\sqrt{m_{22}k_{22}}} = \frac{\pi^4 \eta \omega_0}{6}\frac{c_{22}}{k_{22}} \quad (A_{(0)} \gg h) \tag{35}$$

We refer to Eqs. (34) and (35) as the simplified form of the analytical model for $A_{(0)} \ll h$ and $A_{(0)} \gg h$, respectively.

2.3 The Extension of the Analytical Model to General Three-Dimensional Structures. Since the 3D structures formed via controlled buckling technique usually have a large static deflection amplitude, this paper focuses on the case when $A_{(0)} \gg h$. The half-band width of the buckled ribbon in Eq. (35) can be further written by using the relationship $\varepsilon_{\text{compre}} = \pi^2 A_{(0)}^2/L^2\left(1 + h^2/3A_{(0)}^2\right) \approx \pi^2 A_{(0)}^2/L^2$, as

$$\xi_2^* = \frac{\pi^4 \eta \omega_0}{6}\frac{c_{22}}{k_{22}} = \eta\omega_0\hat{\xi} \tag{36}$$

where $\hat{\xi}$ is the nondimensional half band width of the buckled ribbon as

$$\hat{\xi} = \frac{\pi^4}{6}\frac{c_{22}}{k_{22}} = \frac{4\varepsilon_{\text{compre}} + 2}{7\varepsilon_{\text{compre}} + 3} \tag{37}$$

By using the first-order Taylor expansion, the nondimensional half-band width of the buckled ribbon demonstrated in Eq. (37) can be approximately written as

$$\hat{\xi} \approx \frac{2}{3}\left(1 - \frac{1}{3}\varepsilon_{\text{compre}}\right) \tag{38}$$

Inspired by the structure of the analytical solutions in Eqs. (36) and (38), the nondimensional half-band width $\hat{\xi}$ can be expressed in the form of scaling law by a single-variable function of the compressive strain $\varepsilon_{\text{compre}}$ as

$$\hat{\xi} = \alpha\left(1 + \beta\varepsilon_{\text{compre}}\right) \tag{39}$$

where α and β can be determined by fitting the FEA results of the $\hat{\xi} \sim \varepsilon_{\text{compre}}$ curves. As we show in Sec. 3, the scaling law Eq. (39) applies to the vibration of a variety of 3D structures formed by the compressive buckling technique with viscoelastic materials. In addition, it can be seen from Eq. (36) that this scaling law is independent of structural dimensions and material properties.

3 Examples and Discussions

The analytical model is validated by FEA, as presented in Fig. 2. The FEA were performed using the commercial software ABAQUS. The material was assumed to be a photopatternable epoxy

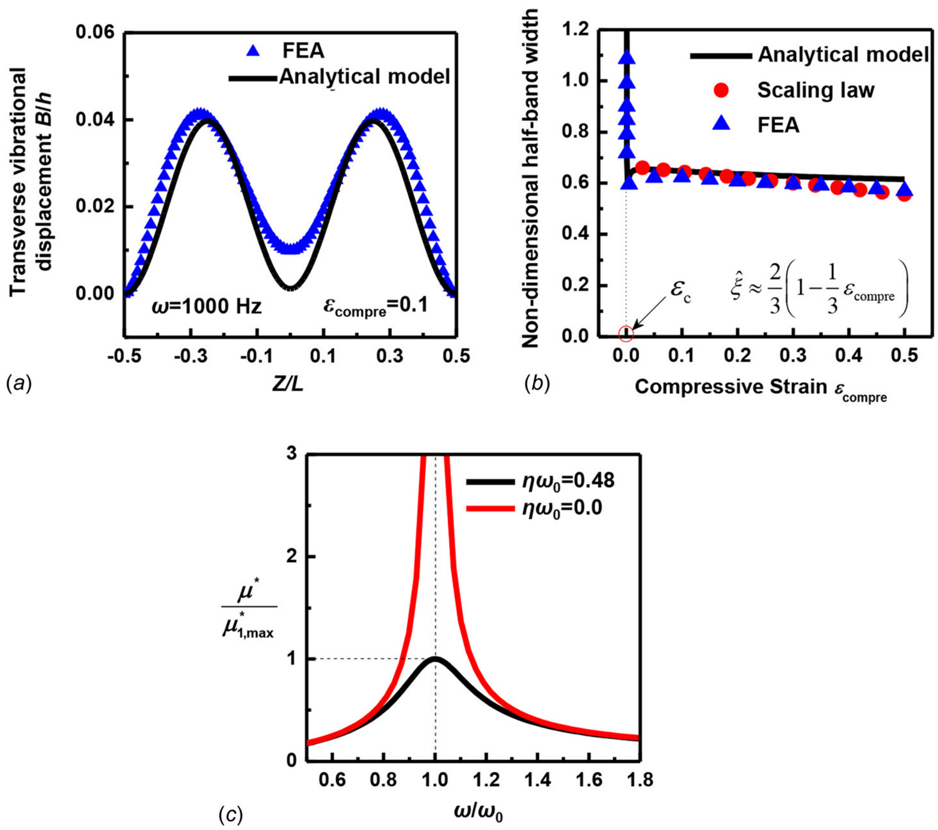

Fig. 2 Finite element analysis validations of the analytical model for the first-order vibration mode: (*a*) transverse vibrational displacement as a function of position, (*b*) the nondimensional half-band width $\hat{\xi}$ as a function of the compressive strain $\varepsilon_{\text{compre}}$, and (*c*) a comparison of the nondimensional velocity responses of the buckled ribbon with and without the viscoelastic damping effect

Name of Structure	2D	$\hat{\xi}$	3D (ε_{compre}=0.2)	$\hat{\xi}$
Buckled ribbon		0.489		0.622
Tent		0.487	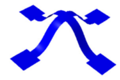	0.608
Table		0.487		0.590

Fig. 3 The nondimensional half-band width of three 3D structures and their 2D precursors

(SU8), a typical polymer used in 3D assembly. The Young's modulus, Poisson's ratio and density of SU8 are $E = 4.02$ GPa, $\nu = 0.22$, and $\rho = 1.2\,\mathrm{g/cm^3}$ [24]. $\eta\omega_0$ is assumed to be a constant to simulate the viscoelastic damping effect of Kelvin–Voigt model based on the data obtained by dynamic mechanical analysis, creep and stress relaxation, and other methods [49,53,54,75,76]. The vibrational displacement and velocity under the harmonic external load were obtained by the steady-state analysis, after importing the shape and stress of the buckled ribbon determined from the post-buckling analysis. The ribbon was discretized by Four-node finite-strain shell elements (S4) and at least 20 elements were implemented along the width direction of the ribbon to guarantee the convergence.

Under a representative compressive strain $\varepsilon_{compre} = 0.1$, the analytical results of the transverse vibrational displacement match well with the FEA results, as shown in Fig. 2(*a*). Figure 2(*b*) gives a comparison of the nondimensional half-band width $\hat{\xi}$ calculated by the general form of the analytical model (Eq. (31)), the scaling law (Eq. (38)), and FEA. The scaling law agrees well with FEA under compressive strain $\varepsilon_{compre} > 0.05$, a typical value used in compressive buckling techniques. The general form of the analytical model agrees well with FEA in a broader range of compressive strain ε_{compre}, even when ε_{compre} is close to the critical strain ε_c. Note that the nondimensional half-band width increases significantly when ε_{compre} decreases to ε_c, which is consistent with the simplified form of the analytical model for $A_{(0)} \ll h$ (Eq. (34)). Further, Fig. 2(*c*) plots a comparison of nondimensional velocity responses of the buckled ribbon with and without the viscoelastic damping effect. A obviously sharp peak of $\mu^*/\mu^*_{1,\max} \sim \omega/\omega_0$ curve occurs at the natural frequency ($\omega/\omega_0 = 1$) for the case without the viscoelastic damping effect, where $\mu^*_{1,\max}$ represents the maximum of velocity response with respect to the frequency when the viscoelastic damping effect is present.

To compare the half-band width of 3D buckled structures with that of their corresponding 2D precursors, the FEA results of three pairs of structures (buckled ribbon, tent, and table) are presented in Fig. 3. The nondimensional half-band widths of these 3D structures are $\sim$25% larger than their 2D precursors. It is also noticed that the nondimensional half-band widths of these 2D structures are almost the same.

Figure 4 shows the variations of the nondimensional half-band width $\hat{\xi}$ of three complex structures (tent, table, and helix) with compressive strain ε_{compre} ranged from 0.05 to 0.30. The relationship of $\hat{\xi}$ versus ε_{compre} can be well modeled by the scaling law in Eq. (39) with proper parameters α and β. The paramters relate the nondimensional half-band width $\hat{\xi}$ to the topology of 2D precursor and the compressive strain ε_{compre}. When ε_{compre} ranges from 0.05 to 0.30, $\hat{\xi}$ decreases by about 5%. For the same compressive

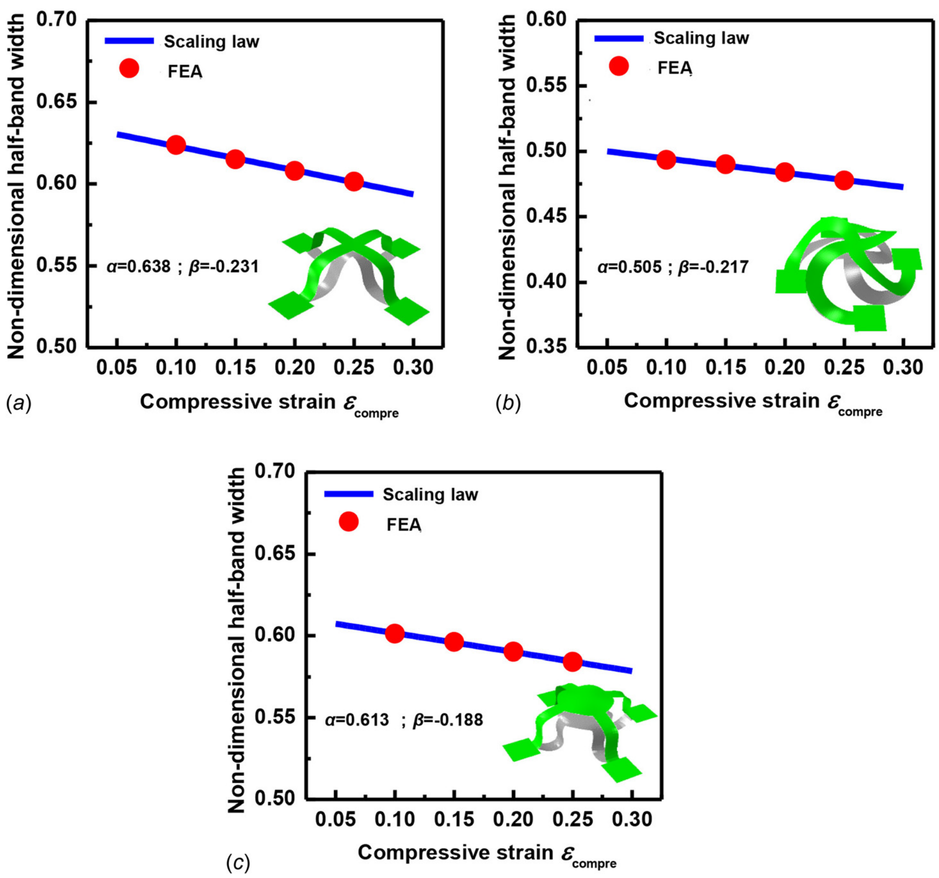

Fig. 4 Extension of the scaling law to representative 3D structures, with validations by FEA: (*a*) tent, (*b*) helix, and (*c*) table

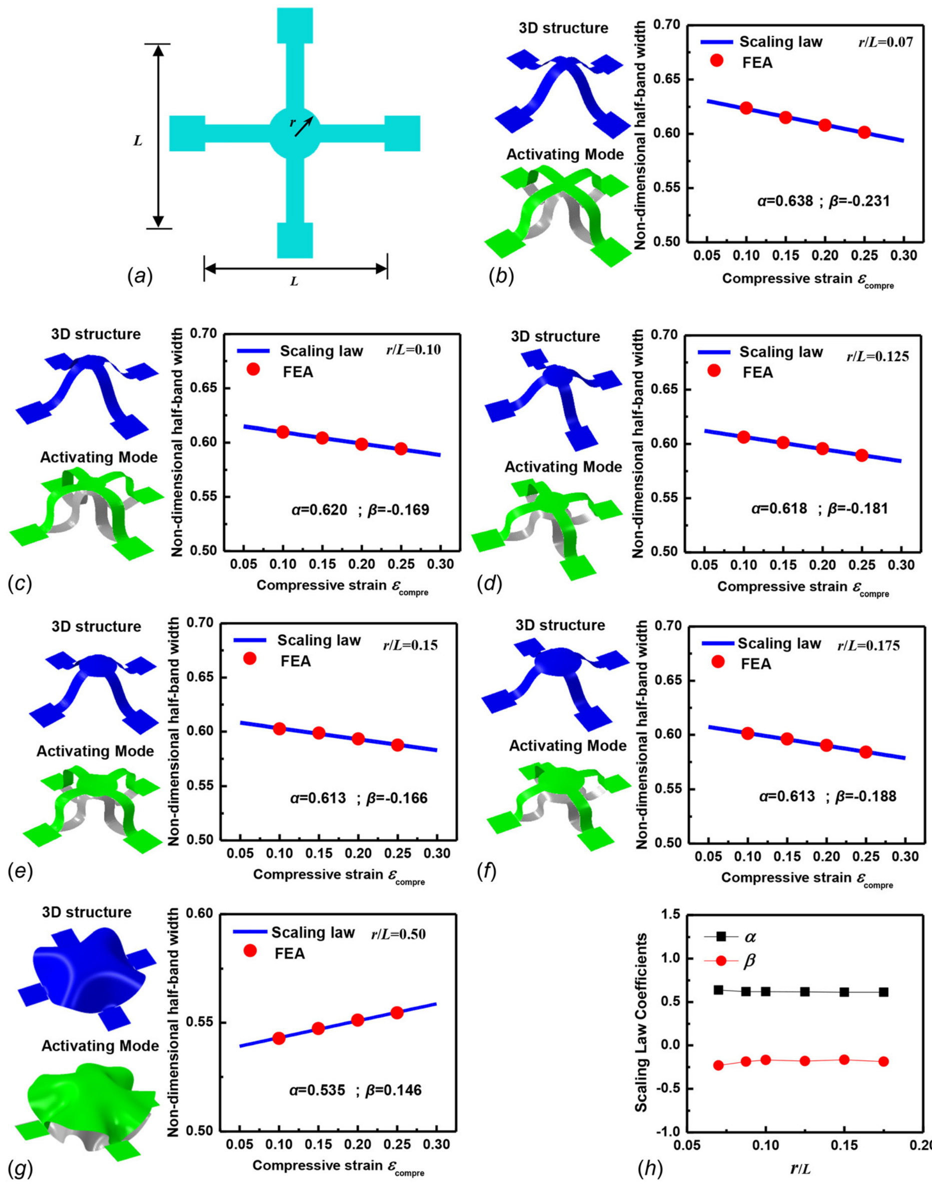

Fig. 5 Extension of the scaling law to 3D table structures with different central circle radii, with validations by FEA: (*a*) illustration of the precursor and geometries, (*b*)–(*g*) the nondimensional half-band width $\hat{\xi}$ as a function of the compressive strain, for different normalized central circle radii (*r*/*L* = 0.07, 0.10, 0.125, 0.15, 0.175, and 0.50) of the 2D precursor, and (*h*) parameters α and β that characterize the scaling law of the nondimensional half-band width, as a function of *r*/*L*

strain, the nondimensional half-band widths of the three structures show about 20% difference among each other. To further illustrate the relationship between $\hat{\xi}$ and the structure shape, we study more 3D structures as shown in Figs. 5 and 6.

Figure 5(*a*) shows the geometry of the table structures with different central circle radii r. The table structure becomes the tent structure when r equals to the ribbon width. Figures 5(*b*)–5(*g*) presents the FEA results of the nondimensional half-band width $\hat{\xi}$ of the first-order mode, when the normalized circle radius r/L ranges from 0.07 to 0.175, as well as a demonstration of $r/L = 0.50$, and the compressive strain $\varepsilon_{\text{compre}}$ ranges from 0.05 to 0.30. The scaling law in Eq. (39) could remarkably characterize the FEA results for all cases with proper parameters α and β, which change slightly with r/L as shown in Fig. 5(*h*).

Similarly, Fig. 6(*a*) shows the geometry of the helix structures with different top angles θ. The helix structure becomes the tent structure when θ is 0 deg. The scaling law in Eq. (39) could also remarkably characterize the FEA results for all cases (Figs. 6(*b*)–6(*g*)) with proper parameters α and β, which change slightly with θ as shown in Fig. 6(*h*).

4 Conclusions

This paper presents a study on the viscoelastic characteristics of 3D structures formed by compressive buckling techniques via an analytical model and the FEA. The Kelvin–Voigt model is introduced to characterize the material viscoelasticity. A validation between the analytical model and FEA is presented, and a scaling law to characterize the half-band width is obtained and extended to more complex 3D structures including tent, table, and helix. Some main conclusions can be drawn as: (1) The nondimensional half-band width of the buckled straight ribbon, tent, and table structures are about 25% larger than that of their 2D precursors. (2) The scaling law relates the half-band width to the structure shape and the compressive strain via two parameters. The model and FEA focus on the vibration when the 3D structure is

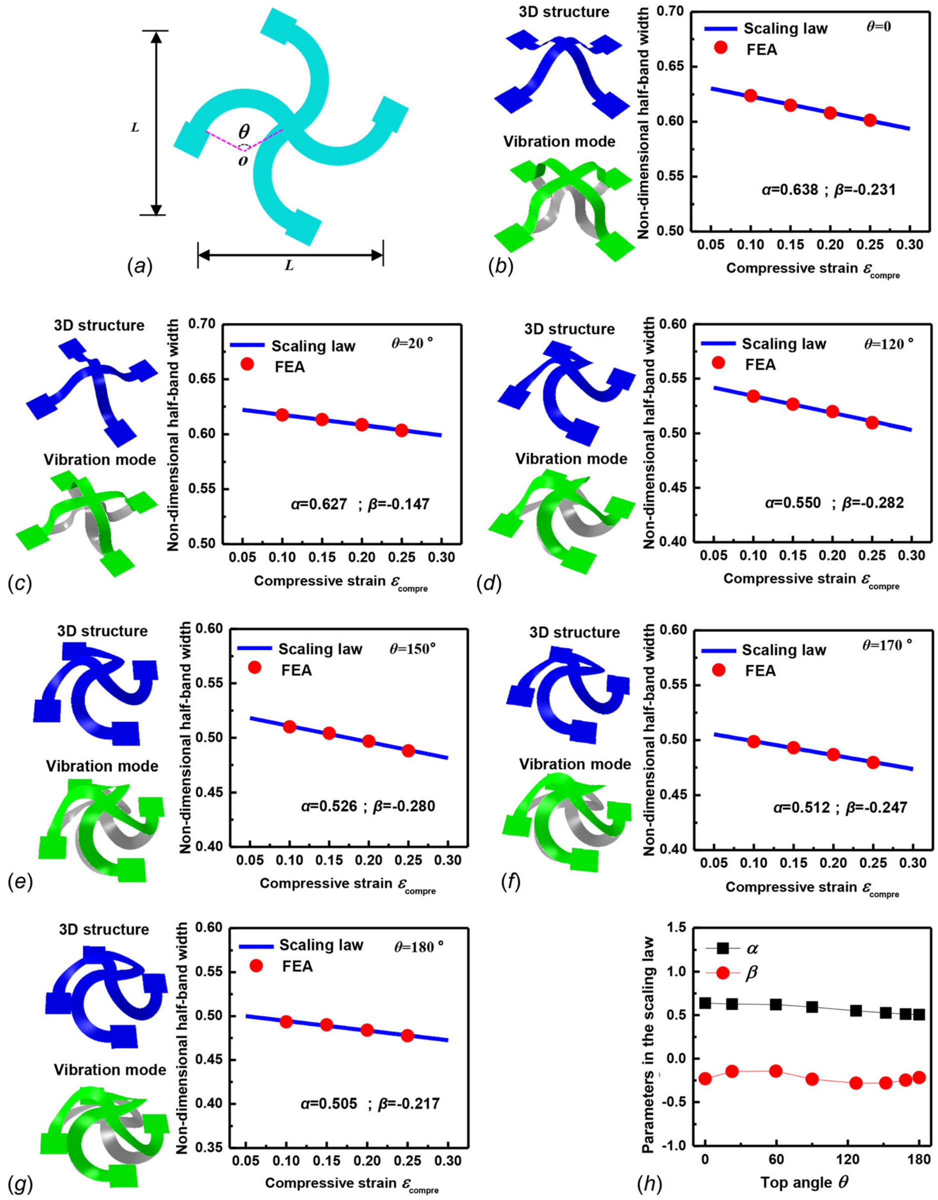

Fig. 6 Extension of the scaling law to 3D helical structures with different top angles, with validations by FEA: (*a*) illustration of the precursor and geometries, (*b*)–(*g*) the nondimensional half-band width $\hat{\xi}$ as a function of the compressive strain, for different top angles ($\theta = 0$ deg, 20 deg, 120 deg, 150 deg, 170 deg, and 180 deg) of the 2D precursor, and (*h*) parameters α and β that characterize the scaling law of the nondimensional half-band width, as a function of θ

transferred on to a rigid base after compressive buckling to remove the soft elastomer. Taking the underlying substrate into the model is a future direction, which may broaden the application to cases when the 3D structure is transferred on to a deformable base such as skin or remains on the soft elastomer. This paper could serve as design guidelines of MEMS for their potential applications in energy harvesting and mechanical sensors.

Acknowledgment

Y. Z. acknowledges the support from the National Natural Science Foundation of China, the National Basic Research Program of China and the Tsinghua National Laboratory for Information Science and Technology. Y. H. acknowledges the support from NSF. H. B. Li thanks the support from China Scholarship Council. This works is also financially supported from National Science Foundation of China (NSFC).

Funding Data

- National Basic Research Program of China (2015CB351900).
- National Natural Science Foundation of China (11722217 and 11732009).
- National Science Foundation (CMMI1400169, CMMI1534120, and CMMI1635443).

Appendix

Using $\Delta \boldsymbol{a} = \mathrm{Im}(\Delta \tilde{\boldsymbol{a}})$ and substituting $\Delta \tilde{\boldsymbol{a}} = \Delta \tilde{\boldsymbol{A}} e^{i\omega t}$ into Eq. (24) leads to

$$\begin{bmatrix} -\omega^2 M_{11} + i\omega C_{11} + K_{11} & -\omega^2 M_{12} \\ -\omega^2 M_{12} & -\omega^2 M_{11} + i\omega C_{22} + K_{22} \end{bmatrix} \begin{bmatrix} \Delta\tilde{A}_{(1)} \\ \Delta\tilde{A}_{(2)} \end{bmatrix} = \boldsymbol{M}\Delta\tilde{\boldsymbol{A}} = \begin{bmatrix} P_0 L \\ P_0 L \end{bmatrix} \tag{A1}$$

Then, by multiplying the inverse coefficients matrix $\boldsymbol{M}^{-1}$ at both sides of Eq. (A1), the solutions of $\Delta\tilde{A}_{(1)}$ and $\Delta\tilde{A}_{(2)}$ can be expressed as

$$\Delta\tilde{A}_{(1)} = B_{r1} + iB_{i1}, \quad \Delta\tilde{A}_{(2)} = B_{r2} + iB_{i2} \tag{A2}$$

where

$$\begin{aligned} B_{r1} &= \frac{-P_0 L\left\{\left[K_{22} + (M_{12} - M_{22})\omega^2\right]T_1 + T_2 C_{22}\omega\right\}}{T_1^2 + T_2^2} \\ B_{i1} &= \frac{-P_0 L\left\{T_1 C_{22}\omega - T_2\left[K_{22} + (M_{12} - M_{22})\omega^2\right]\right\}}{T_1^2 + T_2^2} \\ B_{r2} &= \frac{-P_0 L\left\{\left[K_{11} + (M_{12} - M_{11})\omega^2\right]T_1 + T_2 C_{11}\omega\right\}}{T_1^2 + T_2^2} \\ B_{i2} &= \frac{-P_0 L\left\{T_1 C_{11}\omega - T_2\left[K_{11} + (M_{12} - M_{11})\omega^2\right]\right\}}{T_1^2 + T_2^2} \end{aligned} \tag{A3}$$

where

$$\begin{aligned} T_1 &= \left(M_{12}^2 - M_{11}M_{22}\right)\omega^4 + (K_{11}M_{22} + K_{22}M_{11} + C_{11}C_{22})\omega^2 - K_{11}K_{22} \\ T_2 &= (C_{11}M_{22} + C_{22}M_{11})\omega^3 - (C_{11}K_{22} + C_{22}K_{11})\omega \end{aligned} \tag{A4}$$

Thereby, the solutions of Eq. (24) are obtained as

$$\begin{bmatrix} \Delta a_{(1)} \\ \Delta a_{(2)} \end{bmatrix} = \mathrm{Im}\begin{bmatrix} \Delta\tilde{a}_{(1)} \\ \Delta\tilde{a}_{(2)} \end{bmatrix} = \begin{bmatrix} B_1 \sin(\omega t + \theta_1) \\ B_2 \sin(\omega t + \theta_2) \end{bmatrix} \tag{A5}$$

where, $B_1 = \sqrt{B_{r1}^2 + B_{i1}^2}$, $B_2 = \sqrt{B_{r2}^2 + B_{i2}^2}$, $\tan\theta_1 = B_{i1}/B_{r1}$, and $\tan\theta_2 = B_{i2}/B_{r2}$.

References

[1] Feiner, R., Engel, L., Fleischer, S., Malki, M., Gal, I., Shapira, A., Shacham-Diamand, Y., and Dvir, T., 2016, "Engineered Hybrid Cardiac Patches With Multifunctional Electronics for Online Monitoring and Regulation of Tissue Function," Nat. Mater., **15**(6), pp. 679–685.

[2] Leong, T. G., Randall, C. L., Benson, B. R., Bassik, N., Stern, G. M., and Gracias, D. H., 2009, "Tetherless Thermobiochemically Actuated Microgrippers," Proc. Natl. Acad. Sci., **106**(3), pp. 703–708.

[3] Tian, B., Liu, J., Dvir, T., Jin, L., Tsui, J. H., Qing, Q., Suo, Z., Langer, R., Kohane, D. S., and Lieber, C. M., 2012, "Macroporous Nanowire Nanoelectronic Scaffolds for Synthetic Tissues," Nat. Mater., **11**(11), pp. 986–994.

[4] Muth, J. T., Vogt, D. M., Truby, R. L., Mengüç, Y., Kolesky, D. B., Wood, R. J., and Lewis, J. A., 2014, "Embedded 3D Printing of Strain Sensors Within Highly Stretchable Elastomers," Adv. Mater., **26**(36), pp. 6307–6312.

[5] Gu, L., Tavakoli, M. M., Zhang, D., Zhang, Q., Waleed, A., Xiao, Y., Tsui, K. H., Lin, Y., Liao, L., Wang, J., and Fan, Z., 2016, "3D Arrays of 1024-Pixel Image Sensors Based on Lead Halide Perovskite Nanowires," Adv. Mater., **28**(44), pp. 9713–9721.

[6] Li, X., Lin, Z.-H., Cheng, G., Wen, X., Liu, Y., Niu, S., and Wang, Z. L., 2014, "3D Fiber-Based Hybrid Nanogenerator for Energy Harvesting and as a Self-Powered Pressure Sensor," ACS Nano, **8**(10), pp. 10674–10681.

[7] Xu, L., Gutbrod, S. R., Bonifas, A. P., Su, Y., Sulkin, M. S., Lu, N., Chung, H.-J., Jang, K.-I., Liu, Z., Ying, M., Lu, C., Webb, C., Kim, J. S., Laughner, J. I., Cheng, H., Liu, Y., Ameen, A., Jeong, J. W., Kim, G. T., Huang, Y., Efimov, I. R., and Rogers, J. A., 2014, "3D Multifunctional Integumentary Membranes for Spatiotemporal Cardiac Measurements and Stimulation Across the Entire Epicardium," Nat. Commun., **5**, p. 3329.

[8] Fan, Z., Razavi, H., Do, J-W., Moriwaki, A., Ergen, O., Chueh, Y.-L., Leu, P. W., Ho, J. C., Takahashi, T., and Reichertz, L. A., 2009, "Three-Dimensional Nanopillar-Array Photovoltaics on Low-Cost and Flexible Substrates," Nat. Mater., **8**(8), pp. 648–653.

[9] Valentine, J., Zhang, S., Zentgraf, T., Ulin-Avila, E., Genov, D. A., Bartal, G., and Zhang, X., 2008, "Three-Dimensional Optical Metamaterial With a Negative Refractive Index," Nature, **455**(7211), pp. 376–379.

[10] Xiao, X., Zhou, W., Kim, Y., Ryu, I., Gu, M., Wang, C., Liu, G., Liu, Z., and Gao, H., 2015, "Regulated Breathing Effect of Silicon Negative Electrode for Dramatically Enhanced Performance of Li-Ion Battery," Adv. Funct. Mater., **25**(9), pp. 1426–1433.

[11] Sun, K., Wei, T. S., Ahn, B. Y., Seo, J. Y., Dillon, S. J., and Lewis, J. A., 2013, "3D Printing of Interdigitated Li-Ion Microbattery Architectures," Adv. Mater., **25**(33), pp. 4539–4543.

[12] Ning, H., Pikul, J. H., Zhang, R., Li, X., Xu, S., Wang, J., Rogers, J. A., King, W. P., and Braun, P. V., 2015, "Holographic Patterning of High-Performance on-Chip 3D Lithium-Ion Microbatteries," Proc. Natl. Acad. Sci., **112**(21), pp. 6573–6578.

[13] Nawroth, J. C., Lee, H., Feinberg, A. W., Ripplinger, C. M., McCain, M. L., Grosberg, A., Dabiri, J. O., and Parker, K. K., 2012, "A Tissue-Engineered Jellyfish With Biomimetic Propulsion," Nat. Biotechnol., **30**(8), pp. 792–797.

[14] Bartlett, N. W., Tolley, M. T., Overvelde, J. T., Weaver, J. C., Mosadegh, B., Bertoldi, K., Whitesides, G. M., and Wood, R. J., 2015, "A 3D-Printed, Functionally Graded Soft Robot Powered by Combustion," Science, **349**(6244), pp. 161–165.

[15] Park, S.-J., Gazzola, M., Park, K. S., Park, S., Di Santo, V., Blevins, E. L., Lind, J. U., Campbell, P. H., Dauth, S., Capulli, A. K., Pasqualini, F. S., Ahn, S., Cho, A., Yuan, H., Maoz, B. M., Vijaykumar, R., Choi, J. W., Deisseroth, K., Lauder, G. V., Mahadevan, L., and Parker, K. K., 2016, "Phototactic Guidance of a Tissue-Engineered Soft-Robotic Ray," Science, **353**(6295), pp. 158–162.

[16] Rogers, J., Huang, Y., Schmidt, O. G., and Gracias, D. H., 2016, "Origami MEMS and NEMS," MRS Bull., **41**(2), pp. 123–129.

[17] Liu, Y., Genzer, J., and Dickey, M. D., 2016, "2D or Not 2D": Shape-Programming Polymer Sheets," Prog. Polym. Sci., **52**, pp. 79–106.

[18] Zou, H.-X., Zhang, W.-M., Wei, K.-X., Li, W.-B., Peng, Z.-K., and Meng, G., 2016, "A Compressive-Mode Wideband Vibration Energy Harvester Using a Combination of Bistable and Flextensional Mechanisms," ASME J. Appl. Mech., **83**(12), p. 121005.

[19] Li, W., Torres, D., Díaz, R., Wang, Z., Wu, C., Wang, C., Wang, Z. L., and Sepúlveda, N., 2017, "Nanogenerator-Based Dual-Functional and Self-Powered Thin Patch Loudspeaker or Microphone for Flexible Electronics," Nat. Commun., **8**, p. 15310.

[20] Bao, S., Wang, S., and Wang, B., 2017, "An Improved Fourier–Ritz Method for Analyzing in-Plane Free Vibration of Sectorial Plates," ASME J. Appl. Mech., **84**(9), p. 091001.

[21] Yuan, J., Wei, X., and Huang, Y., 2017, "Exact Solutions for Nonaxisymmetric Vibrations of Radially Inhomogeneous Circular Mindlin Plates With Variable Thickness," ASME J. Appl. Mech., **84**(7), p. 071003.

[22] Li, D., Zheng, Z. L., and Todd, M. D., 2018, "Nonlinear Vibration of Orthotropic Rectangular Membrane Structures Including Modal Coupling," ASME J. Appl. Mech., **85**(6), p. 061004.

[23] Mao, X.-Y., Ding, H., and Chen, L.-Q., 2017, "Vibration of Flexible Structures Under Nonlinear Boundary Conditions," ASME J. Appl. Mech., **84**(11), p. 111006.

[24] Wang, H., Ning, X., Li, H., Luan, H., Xue, Y., Yu, X., Fan, Z., Li, L., Rogers, J. A., Zhang, Y., and Huang, Y., 2018, "Vibration of Mechanically-Assembled 3D Microstructures Formed by Compressive Buckling," J. Mech. Phys. Solids, **112**, pp. 187–208.

[25] Xu, S., Yan, Z., Jang, K.-I., Huang, W., Fu, H., Kim, J., Wei, Z., Flavin, M., McCracken, J., Wang, R., Badea, A., Liu, Y., Xiao, D., Zhou, G., Lee, J., Chung, H. U., Cheng, H., Ren, W., Banks, A., Li, X., Paik, U., Nuzzo, R. G., Huang, Y., Zhang, Y., and Rogers, J. A., 2015, "Assembly of Micro/Nanomaterials Into Complex, Three-Dimensional Architectures by Compressive Buckling," Science, **347**(6218), pp. 154–159.

[26] Zhang, Y., Yan, Z., Nan, K., Xiao, D., Liu, Y., Luan, H., Fu, H., Wang, X., Yang, Q., Wang, J., Ren, W., Si, H., Liu, F., Yang, L., Li, H., Wang, J., Guo, X., Luo, H., Wang, L., Huang, Y., and Rogers, J. A., 2015, "A Mechanically Driven Form of Kirigami as a Route to 3D Mesostructures in Micro/Nanomembranes," Proc. Natl. Acad. Sci., **112**(38), pp. 11757–11764.

[27] Fu, H., Nan, K., Bai, W., Huang, W., Bai, K., Lu, L., Zhou, C., Liu, Y., Liu, F., Wang, J., Han, M., Yan, Z., Luan, H., Zhang, Y., Zhang, Y., Zhao, J., Cheng, X., Li, M., Lee, J. W., Liu, Y., Fang, D., Li, X., Huang, Y., Zhang, Y., and Rogers, J. A., 2018, "Morphable 3D Mesostructures and Microelectronic Devices by Multistable Buckling Mechanics," Nat. Mater., **17**(3), pp. 268–276.

[28] Yan, Z., Zhang, F., Liu, F., Han, M., Ou, D., Liu, Y., Lin, Q., Guo, X., Fu, H., Xie, Z., Gao, M., Huang, Y., Kim, J. H., Qiu, Y., Nan, K., Kim, J., Gutruf, P., Luo, H., Zhao, A., Hwang, K. C., Huang, Y., Zhang, Y., and Rogers, J. A., 2016, "Mechanical Assembly of Complex, 3D Mesostructures From Releasable Multilayers of Advanced Materials," Sci. Adv., **2**(9), p. e1601014.

[29] Zhang, Y., Zhang, F., Yan, Z., Ma, Q., Li, X., Huang, Y., and Rogers, J. A., 2017, "Printing, Folding and Assembly Methods for Forming 3D Mesostructures in Advanced Materials," Nat. Rev. Mater., **2**(4), p. 17019.

[30] Danielson, C., Mehrnezhad, A., YekrangSafakar, A., and Park, K., 2017, "Fabrication and Characterization of Self-Folding Thermoplastic Sheets Using Unbalanced Thermal Shrinkage," Soft Matter, **13**(23), pp. 4224–4230.

[31] Bauhofer, A. A., Krödel, S., Rys, J., Bilal, O. R., Constantinescu, A., and Daraio, C., 2017, "Harnessing Photochemical Shrinkage in Direct Laser Writing for Shape Morphing of Polymer Sheets," Adv. Mater., **29**(42), p. 1703024.

[32] Cools, J., Jin, Q., Yoon, E., Burbano, D. A., Luo, Z., Cuypers, D., Callewaert, G., Braeken, D., and Gracias, D. H., 2018, "A Micropatterned Multielectrode

Shell for 3D Spatiotemporal Recording From Live Cells," Adv. Sci., **5**(4), p. 1700731.
[33] Zhao, R., and Zhao, X., 2017, "Multimodal Surface Instabilities in Curved Film–Substrate Structures," ASME J. Appl. Mech., **84**(8), p. 081001.
[34] Auguste, A., Jin, L., Suo, Z., and Hayward, R. C., 2017, "Post-Wrinkle Bifurcations in Elastic Bilayers With Modest Contrast in Modulus," Extreme Mech. Lett., **11**, pp. 30–36.
[35] Liao, X., Xiao, J., Ni, Y., Li, C., and Chen, X., 2017, "Self-Assembly of Islands on Spherical Substrates by Surface Instability," ACS Nano, **11**(3), pp. 2611–2617.
[36] Vinay, T. V., Banuprasad, T. N., George, S. D., Varghese, S., and Varanakkottu, S. N., 2017, "Additive-Free Tunable Transport and Assembly of Floating Objects at Water-Air Interface Using Bubble-Mediated Capillary Forces," Adv. Mater. Interfaces, **4**(7), p. 1601231.
[37] Hure, J., and Audoly, B., 2013, "Capillary Buckling of a Thin Film Adhering to a Sphere," J. Mech. Phys. Solids, **61**(2), pp. 450–471.
[38] Brubaker, N., and Lega, J., 2016, "Capillary-Induced Deformations of a Thin Elastic Sheet," Philos. Trans. R. Soc. London A, **374**(2066), p. 20150169.
[39] Liu, C., Schauff, J., Joung, D., and Cho, J. H., 2017, "Remotely Controlled Microscale 3D Self-Assembly Using Microwave Energy," Adv. Mater. Technol., **2**(8), p. 1700035.
[40] Cui, J., Yao, S., Huang, Q., Adams, J. G., and Zhu, Y., 2017, "Controlling the Self-Folding of a Polymer Sheet Using a Local Heater: The Effect of the Polymer–Heater Interface," Soft Matter, **13**(21), pp. 3863–3870.
[41] Xiuting, S., Zhang, S., Xu, J., and Wang, F., 2018, "Dynamical Analysis and Realization of an Adaptive Isolator," ASME J. Appl. Mech., **85**(1), p. 011002.
[42] Eichler, A., Moser, J., Chaste, J., Zdrojek, M., Wilson-Rae, I., and Bachtold, A., 2011, "Nonlinear Damping in Mechanical Resonators Made From Carbon Nanotubes and Graphene," Nat. Nanotechnol., **6**(6), pp. 339–342.
[43] Unterreithmeier, Q. P., Faust, T., and Kotthaus, J. P., 2010, "Damping of Nanomechanical Resonators," Phys. Rev. Lett., **105**(2), p. 027205.
[44] Louhghalam, A., Pellenq, R. J.-M., and Ulm, F.-J., 2018, "Thermalizing and Damping in Structural Dynamics," ASME J. Appl. Mech., **85**(8), p. 081001.
[45] Sun, T. L., Kurokawa, T., Kuroda, S., Ihsan, A. B., Akasaki, T., Sato, K., Haque, M. A., Nakajima, T., and Gong, J. P., 2013, "Physical Hydrogels Composed of Polyampholytes Demonstrate High Toughness and Viscoelasticity," Nat. Mater., **12**(10), pp. 932–937.
[46] Khan, A. S., Lopez-Pamies, O., and Kazmi, R., 2006, "Thermo-Mechanical Large Deformation Response and Constitutive Modeling of Viscoelastic Polymers Over a Wide Range of Strain Rates and Temperatures," Int. J. Plasticity, **22**(4), pp. 581–601.
[47] Bauer, F., Denneler, S., and Willert-Porada, M., 2005, "Influence of Temperature and Humidity on the Mechanical Properties of Nafion® 117 Polymer Electrolyte Membrane," J. Polym. Sci. Part B: Polym. Phys., **43**(7), pp. 786–795.
[48] Kim, B., Hopcroft, M. A., Candler, R. N., Jha, C. M., Agarwal, M., Melamud, R., Chandorkar, S. A., Yama, G., and Kenny, T. W., 2008, "Temperature Dependence of Quality Factor in MEMS Resonators," J. Microelectromech. Syst., **17**(3), pp. 755–766.
[49] Chung, S., and Park, S., 2013, "Effects of Temperature on Mechanical Properties of SU-8 Photoresist Material," J. Mech. Sci. Technol., **27**(9), pp. 2701–2707.
[50] Towler, B. W., Rupp, C. J., Cunningham, A. B., and Stoodley, P., 2003, "Viscoelastic Properties of a Mixed Culture Biofilm From Rheometer Creep Analysis," Biofouling, **19**(5), pp. 279–285.
[51] Lu, B., Lamnawar, K., Maazouz, A., and Zhang, H., 2016, "Revealing the Dynamic Heterogeneity of PMMA/PVDF Blends: From Microscopic Dynamics to Macroscopic Properties," Soft Matter, **12**(13), pp. 3252–3264.
[52] Wouters, K., Gijsenbergh, P., and Puers, R., 2011, "Comparison of Methods for the Mechanical Characterization of Polymers for MEMS Applications," J. Micromech. Microeng., **21**(11), p. 115027.
[53] Schiffmann, K. I., and Brill, C., 2007, "Testing the Viscoelastic Properties of SU8 Photo Resist Thin Films at Different Stages of Processing by Nanoindentation Creep and Stress Relaxation," Int. J. Mater. Res., **98**(5), pp. 397–403.
[54] Xu, T., Yoo, J. H., Babu, S., Roy, S., Lee, J.-B., and Lu, H., 2016, "Characterization of the Mechanical Behavior of SU-8 at Microscale by Viscoelastic Analysis," J. Micromech. Microeng., **26**(10), p. 105001.
[55] VanLandingham, M. R., Chang, N. K., Drzal, P., White, C. C., and Chang, S. H., 2005, "Viscoelastic Characterization of Polymers Using Instrumented Indentation—Part I: Quasi-Static Testing," J. Polym. Sci. Part B: Polym. Phys., **43**(14), pp. 1794–1811.
[56] Jandak, M., Neuzil, T., Schneider, M., and Schmid, U., 2016, "Investigation on Different Damping Mechanisms on the Q Factor of MEMS Resonators," Procedia Eng., **168**, pp. 929–932.
[57] Torvik, P. J., 2011, "On Estimating System Damping From Frequency Response Bandwidths," J. Sound Vib., **330**(25), pp. 6088–6097.
[58] Fang, X., Chuang, K.-C., Jin, X., and Huang, Z., 2018, "Band-Gap Properties of Elastic Metamaterials With Inerter-Based Dynamic Vibration Absorbers," ASME J. Appl. Mech., **85**(7), p. 071010.
[59] Marynowski, K., 2002, "Non-Linear Dynamic Analysis of an Axialy Moving Viscoelastic Beam," J. Theor. Appl. Mech., **40**(2), pp. 465–482.
[60] Arefi, M., and Zenkour, A. M., 2017, "Nonlocal Electro-Thermo-Mechanical Analysis of a Sandwich Nanoplate Containing a Kelvin–Voigt Viscoelastic Nanoplate and Two Piezoelectric Layers," Acta Mech., **228**(2), pp. 475–493.
[61] Rossikhin, Y. A., and Shitikova, M. V., 2011, "The Analysis of the Impact Response of a Thin Plate Via Fractional Derivative Standard Linear Solid Model," J. Sound Vib., **330**(9), pp. 1985–2003.
[62] Ghayesh, M. H., 2012, "Nonlinear Dynamic Response of a Simply-Supported Kelvin–Voigt Viscoelastic Beam, Additionally Supported by a Nonlinear Spring," Nonlinear Anal.: Real World Appl., **13**(3), pp. 1319–1333.
[63] Mahmoodi, S. N., Jalili, N., and Khadem, S. E., 2008, "An Experimental Investigation of Nonlinear Vibration and Frequency Response Analysis of Cantilever Viscoelastic Beams," J. Sound Vib., **311**(3–5), pp. 1409–1419.
[64] Kolahchi, R., 2017, "A Comparative Study on the Bending, Vibration and Buckling of Viscoelastic Sandwich Nano-Plates Based on Different Nonlocal Theories Using DC, HDQ and DQ Methods," Aerosp. Sci. Technol., **66**, pp. 235–248.
[65] Tseng, W.-Y., and Dugundji, J., 1971, "Nonlinear Vibrations of a Buckled Beam Under Harmonic Excitation," ASME J. Appl. Mech., **38**(2), pp. 467–476.
[66] Cottone, F., Gammaitoni, L., Vocca, H., Ferrari, M., and Ferrari, V., 2012, "Piezoelectric Buckled Beams for Random Vibration Energy Harvesting," Smart Mater. Struct., **21**(3), p. 035021.
[67] Yan, Z., Han, M., Shi, Y., Badea, A., Yang, Y., Kulkarni, A., Hanson, E., Kandel, M. E., Wen, X., Zhang, F., Luo, Y., Lin, Q., Zhang, H., Guo, X., Huang, Y., Nan, K., Jia, S., Oraham, A. W., Mevis, M. B., Lim, J., Guo, X., Gao, M., Ryu, W., Yu, K. J., Nicolau, B. G., Petronico, A., Rubakjin, S. S., Lou, J., Ajayan, P. M., Thornton, K., Popescu, G., Fang, D., Sweedler, J. V., Braun, P. V., Zhang, H., Nuzzo, R. G., Huang, Y., Zhang, Y., and Rogers, J. A., 2017, "Three-Dimensional Mesostructures as High-Temperature Growth Templates, Electronic Cellular Scaffolds, and Self-Propelled Microrobots," Proc. Natl. Acad. Sci., **114**(45), pp. E9455–E9464.
[68] Su, Y., Wu, J., Fan, Z., Hwang, K.-C., Song, J., Huang, Y., and Rogers, J. A., 2012, "Postbuckling Analysis and Its Application to Stretchable Electronics," J. Mech. Phys. Solids, **60**(3), pp. 487–508.
[69] Fan, Z., Zhang, Y., Ma, Q., Zhang, F., Fu, H., Hwang, K.-C., and Huang, Y., 2016, "A Finite Deformation Model of Planar Serpentine Interconnects for Stretchable Electronics," Int. J. Solids Struct., **91**, pp. 46–54.
[70] Fan, Z., Wu, J., Ma, Q., Liu, Y., Su, Y., and Hwang, K.-C., 2017, "Post-Buckling Analysis of Curved Beams," ASME J. Appl. Mech., **84**(3), p. 031007.
[71] Fan, Z., Hwang, K.-C., Rogers, J. A., Huang, Y., and Zhang, Y., 2018, "A Double Perturbation Method of Postbuckling Analysis in 2D Curved Beams for Assembly of 3D Ribbon-Shaped Structures," J. Mech. Phys. Solids, **111**, pp. 215–238.
[72] Ko, H. C., Shin, G., Wang, S., Stoykovich, M. P., Lee, J. W., Kim, D. H., Ha, J. S., Huang, Y., Hwang, K. C., and Rogers, J. A., 2009, "Curvilinear Electronics Formed Using Silicon Membrane Circuits and Elastomeric Transfer Elements," Small, **5**(23), pp. 2703–2709.
[73] Zhu, L., and Chen, X., 2017, "Delamination-Based Measurement and Prediction of the Adhesion Energy of Thin Film/Substrate Interfaces," J. Eng. Mater. Technol., **139**(2), p. 021021.
[74] Şimşek, M., and Kocatürk, T., 2009, "Nonlinear Dynamic Analysis of an Eccentrically Prestressed Damped Beam Under a Concentrated Moving Harmonic Load," J. Sound Vib., **320**(1–2), pp. 235–253.
[75] Schoeberle, B., Wendlandt, M., and Hierold, C., 2008, "Long-Term Creep Behavior of SU-8 Membranes: Application of the Time–Stress Superposition Principle to Determine the Master Creep Compliance Curve," Sens. Actuators A: Phys., **142**(1), pp. 242–249.
[76] Banks, H. T., and Inman, D., 1991, "On Damping Mechanisms in Beams," ASME J. Appl. Mech., **58**(3), pp. 716–723.